RSC Advances

PAPER

View Article Online
View Journal | View Issue

Cite this: *RSC Adv.*, 2026, **16**, 3791

Correlated structural, vibrational and dielectric properties of the $[(C_4H_9)_4N]_2CoBr_4$ compound: origin of low-frequency polarization

Ridha Briki,[a] Khawla Ben Brahim,[a] Malika Ben Gzaiel,*[ab] Nourah A. Alsobai,[c] Walid Rekik[d] and Abderrazek Oueslati[a]

Organic–inorganic hybrid materials based on divalent metal halides constitute versatile platforms for tuning their physicochemical properties, with potential applications in optoelectronics, energy storage, and dielectric devices. Here, we present the first synthesis and complete characterization of $[(C_4H_9)_4N]_2CoBr_4$, a novel halogenocobaltate(II) compound. Hirshfeld surface analysis and single-crystal X-ray diffraction reveal a monoclinic structure composed of layered tetrabutylammonium cations and tetrahedral $[CoBr_4]^{2-}$ units stabilized by strong C–H···Br interactions. The integrity of the organic and inorganic components is verified by vibrational spectroscopy (FT-IR and Raman). DSC analysis revealed the existence of two phase transitions at 335 K and 345 K. Electrical and dielectric tests, performed between 313 K and 353 K, demonstrated a phase transition around $T = 338$ K, as well as non-Debye relaxation processes, thermally activated charge transport, and semiconducting properties. At low frequencies, the dielectric permittivity reaches exceptionally high values ($\varepsilon' \approx 10^5$), highlighting the strong dielectric response of this material and its potential relevance for functional dielectric and energy-storage applications. This study expands the family of functional halogenocobaltates(II) and provides valuable insights into the structure–property relationships that govern hybrid materials.

Received 5th December 2025
Accepted 19th December 2025

DOI: 10.1039/d5ra09416j

rsc.li/rsc-advances

1. Introduction

Organic–inorganic hybrid materials based on divalent and trivalent metal halides have attracted increasing interest in recent years due to their structural adaptability and the combination of their controllable physicochemical characteristics. Offering promising prospects in optoelectronics, information storage, dielectric switching, and other advanced technologies, these materials lie at the intersection of basic and applied research.[1,2] Their simple synthesis, often achievable at room temperature with a low environmental impact, reinforces their importance for the design of sustainable materials, in addition to their functional potential.[3–8] The halogenocobaltate(II) class is particularly interesting in this regard. Their structural and functional characteristics are strongly influenced by their ability to form hydrogen bonds with organic cations, as well as by the size and symmetry of these cations. When Co(II) is in tetrahedral coordination with halide ligands, the lifting of the degeneracy of its crystal field induces unique electronic characteristics that directly impact its optical, electrical, and dielectric properties. Several tetrahalocobaltate compounds have been described, including $[N(C_3H_7)_4]_2CoBr_4$,[9] $[(C_6H_9N_2)]_2CoCl_4$,[10] $[N(CH_3)_4]_2CoBr_4$,[11] and $[N(C_3H_7)_4]_2CoCl_4$,[12] illustrating how slight structural modifications can significantly alter their physical properties.

Numerous publications are devoted to alkylammonium-type aliphatic cation hybrid compounds, characterized by the general formula A_yMX_4, where A represents an organic cation, $y = 1$ or 2, M a transition metal (Co, Cu, Zn, Fe, Cd, Hg, Mn, *etc.*) and X a halide (Cl, Br, I). These materials are attracting increasing interest due to the wide diversity of their structures and their tunable physicochemical properties, closely linked to the nature of the central metal and the alkylammonium cation. Numerous analogous compounds have been described in the literature, including $[N(C_3H_7)_4]_2HgBr_4$,[13] $[N(C_3H_7)_4]_2ZnBr_4$,[14] $[N(CH_3)_4]_2CoCl_4$,[15] $[N(C_2H_5)_4]_2Cu_2I_4$ (ref. 16) and $[(C_4H_9)_4P]_2Cd_2Cl_6$.[17] These examples illustrate the structural richness and wide variety of architectures present in alkylammonium tetrahalometalates(II).

In this study, we present the synthesis and characterization of a new tetrahalocobaltate(II) compound, $[(C_4H_9)_4N]_2CoBr_4$. Subsequently, single-crystal X-ray diffraction, Hirshfeld surface analysis, thermal scanning calorimetry (DSC), and complex

[a]*University of Sfax, Faculty of Sciences, Laboratory of Spectroscopic Characterization and Optical Materials, BP1171, 3018 Sfax, Tunisia. E-mail: bengzaiel_malika@yahoo.com*

[b]*University of Gafsa, Higher Institute of Social Sciences and Education, Gafsa, 2119, Tunisia*

[c]*Department of Physics, College of Science, Taif University, P. O. Box 11099, Taif, 21944, Saudi Arabia*

[d]*University of Sfax, Faculty of Sciences, Laboratory Physical-Chemistry of the Solid State, Chemistry Department, Tunisia*

impedance spectroscopy were employed to examine its structure and functional properties in detail. The results obtained expand the family of functional halogenocobaltates(II) and shed new light on the relationship between organic chain length, supramolecular organization, and phase transition behavior in hybrid materials.

2. Experimental section

2.1. Synthesis

The process of slow evaporation was used to make ($[(C_4H_9)_4N]_2$)$CoBr_4$. Stoichiometric quantities of $[(C_4H_9)_4N]Br$ (0.29 g, 9.1×10^{-4} mol) and $CoBr_2$ (0.1 g, 4.5×10^{-4} mol) were dissolved in aqueous solution while being continuously swirled. The reaction's trajectory is described by the following equation:

$$2[(C_4H_9)_4N]Br + CoBr_2 \rightarrow ([(C_4H_9)_4N]_2)CoBr_4$$

The homogeneous solution obtained was allowed to evaporate gradually at room temperature. After about a week, high-quality single crystals of $[(C_4H_9)_4N]_2CoBr_4$ were produced, exhibiting a prismatic shape and a blue color.

2.2. Single-crystal X-ray crystallography

A high-quality single crystal of ($[(C_4H_9)_4N]_2$)$CoBr_4$ was carefully selected under a polarizing microscope, mounted with adhesive, and measured at 296 K on a four-circle Bruker APEX II area-detector diffractometer. Reflection data were collected using graphite-monochromated Mo Kα radiation ($\lambda = 0.71073$ Å). Intensity data were processed with the APEX 2 program,[18] and empirical multi-scan absorption corrections were applied using SADABS.[19]

The crystal structure, belonging to the monoclinic system with centrosymmetric space group $P2_1/c$, was solved by direct methods using SHELXT-2018 (ref. 20) within the WINGX suite.[21] All non-hydrogen atoms were refined anisotropically, while hydrogen atom positions were geometrically generated using the HFIX instruction in SHELXL-2014,[22] with C–H distances constrained to 0.96 or 0.97 Å.

Final structure refinement yielded satisfactory reliability factors: $R_1 = 0.0556$ and $wR_2 = 0.1650$. Crystal structure representations were produced using Diamond 3.2.[23] Pertinent details of the crystal structure of $(C_{16}H_{36}N)_2[CoBr_4]$ are summarized in Table 1, while selected bond distances, bond angles, and hydrogen-bond parameters are listed in Tables 2 and 3, respectively.

Supplementary crystallographic data in CIF format are available from the Cambridge Crystallographic Data Centre (CCDC 2419610) as SI.

2.3. Hirshfeld surface

These surfaces define the volume of space where a molecule's electron density dominates over that of its neighboring molecules.[24,25] For each point on the surface, two distances are defined:

Table 1 Crystal data and structure refinement for $[(C_4H_9)_4N]_2CoBr_4$ at 300 K

Formula	$[(C_4H_9)_4N]_2CoBr_4$
Color/shape	Blue/prism
Formula weight (g mol^{-1})	863.48
Crystal system	Monoclinic
Space group	$P2_1/c$
Density	1.363
Crystal size (mm)	0.23 × 0.18 × 0.13
Temperature (K)	296(2)
Diffractometer	Bruker APEX II
a (Å)	16.1580(2)
b (Å)	16.6083(2)
c (Å)	16.9298(2)
β (°)	112.185(3)
V (Å^3)	4206.89(13)
Z	4
Radiation type	Mo Kα (0.71073 Å)
Absorption correction	Multi-scan
θ range for data collection (°)	$1.786 \leq \theta \leq 26.022$
Measured reflections	74 808
Independent reflections	8288
Observed data [$I > 2\sigma(I)$]	3876
Index ranges	$h = -19$ to 19, $k = -20$ to 20, $l = -20$ to 20
$F(000)$	1780
Number of parameters	360
R_1	0.0556
wR_2	0.1650
Goof	1.002

(1) d_i, the distance from the point to the nearest nucleus inside the surface, (2) d_e, the distance to the nearest nucleus outside the surface.

The normalized contact distance (d_{norm}) is obtained from these values as follows:

$$d_{norm} = \frac{d_i - r_i^{vdW}}{r_i^{vdW}} + \frac{d_e - r_e^{vdW}}{r_e^{vdW}} \quad (1)$$

with r_i^{vdW} and r_e^{vdW} are the van der Waals radii of the respective atoms. The d_{norm} values are visualized using a red-white-blue color scheme: negative values (red) indicate contacts shorter than the sum of van der Waals radii, zero (white) corresponds to contacts near the van der Waals separation, and positive values (blue) indicate longer contacts.[26]

Additionally, 2D fingerprint plots, which combine d_i and d_e, allow quantification of the contributions of different types of intermolecular interactions.[27]

2.4. Vibrational analysis

At room temperature, the infrared spectrum of the $[(C_4H_9)_4N]_2CoBr_4$ compound was recorded using a PerkinElmer FT-IR 1000 spectrometer over the frequency range 400–3500 cm^{-1}, with a resolution of 0.5 cm^{-1}. The Raman scattering spectrum (50–3500 cm^{-1}) was obtained using a Horiba Jobin-Yvon T64000 spectrometer (ISA, Jobin Yvon) with a 532 nm excitation wavelength.

Table 2 Selected bond distances (Å) and angles (°) for $[N(C_4H_9)_4]_2CoBr_4$

Distances (Å)		Angles (°)	
Co1–Br4	2.3953(12)	Br4–Co1–Br3	111.65(5)
Co1–Br3	2.3994(11)	Br4–Co1–Br2	112.66(5)
Co1–Br2	2.4067(11)	Br3–Co1–Br2	106.94(4)
Co1–Br1	2.4253(10)	Br4–Co1–Br1	106.63(4)
N1–C9	1.510(8)	Br3–Co1–Br1	110.39(4)
N1–C13	1.517(8)	Br2–Co1–Br1	108.56(4)
N1–C5	1.522(8)	C9–N1–C13	112.0(5)
N1–C1	1.530(8)	C9–N1–C5	109.0(5)
C1–C2	1.499(9)	C13–N1–C5	108.9(5)
C2–C3	1.500(10)	C9–N1–C1	108.2(5)
C3–C4	1.470(10)	C13–N1–C1	108.8(5)
C5–C6	1.512(10)	C5–N1–C1	110.0(5)
C6–C7	1.5004(10)	C2–C1–N1	117.5(5)
C7–C8	1.4988(10)	C1–C2–C3	110.8(6)
C9–C10	1.504(9)	C4–C3–C2	114.3(7)
C10–C11	1.541(11)	C6–C5–N1	116.6(6)
C11–C12	1.468(12)	C7–C6–C5	126.0(9)
C13–C14	1.498(9)	C8–C7–C6	117.7(13)
C14–C15	1.501(10)	C10–C9–N1	116.1(6)
C15–C16	1.483(12)	C9–C10–C11	109.6(7)
N2–C17	1.491(9)	C12–C11–C10	114.2(9)
N2–C21	1.514(10)	C14–C13–N1	115.5(6)
N2–C29	1.515(11)	C13–C14–C15	111.6(7)
N2–C25	1.517(9)	C16–C15–C14	113.1(8)
C17–C18	1.488(11)	C17–N2–C21	110.9(6)
C18–C19	1.589(12)	C17–N2–C29	97.2(6)
C19–C20	1.456(15)	C21–N2–C29	115.9(7)
C21–C22	1.510(11)	C17–N2–C25	112.9(6)
C22–C23	1.542(13)	C21–N2–C25	105.8(6)
C23–C24	1.486(15)	C29–N2–C25	114.2(6)
C25–C27	1.502(10)	C18–C17–N2	116.3(7)
C26–C28	1.496(12)	C17–C18–C19	111.5(8)
C26–C27	1.512(11)	C20–C19–C18	110.1(10)
C29–C30	1.4987(10)	C22–C21–N2	117.7(7)
C30–C31	1.551(13)	C21–C22–C23	108.9(8)
C31–C32	1.432(12)	C24–C23–C22	110.7(10)
		C27–C25–N2	116.6(7)
		C28–C26–C27	112.3(8)
		C25–C27–C26	109.2(7)
		C30–C29–N2	115.9(9)
		C29–C30–C31	110.3(9)
		C32–C31–C30	124.5(10)

Table 3 Hydrogen bond parameters for $[N(C_4H_9)_4]_2CoBr_4$[a]

D–H···A	D–H	H···A	D···A	D–H···A
C1–H1A···Br1[i]	0.97	3.10	3.951(7)	147.5
C5–H5A···Br2	0.97	3.05	3.748(7)	130.2
C6–H6B···Br1[i]	0.97	3.12	4.020(8)	154.3
C13–H13A···Br3[i]	0.97	3.03	3.988(7)	169.3
C13–H13B···Br3[ii]	0.97	2.96	3.893(7)	161.4
C21–H21B–Br1[iii]	0.97	3.14	4.096(9)	169.4
C25–H25B–Br1[iv]	0.97	3.03	3.965(8)	162.1
C29–H29A–Br4	0.97	2.95	3.772(9)	143.6

[a] Symmetry codes: [i] $-x+/2, y+1/2, -z+1/2$; [ii] $x, -y+1/2, z-1/2$; [iii] $-x+1, y+1/2, -z+1/2$; [iv] $x, -y+1/2, z+1/2$.

2.5. Thermal analysis DSC

Differential scanning calorimetry, DSC, was executed with a PerkinElmer DSC-7 instrument in a temperature range from 320 K to 360 K with a 5 K min^{-1} rate.

2.6. Impedance spectroscopy

Under uniaxial pressure, the crystals were crushed and formed into a cylindrical pellet that measured 8 mm in diameter and 1.1 mm in thickness. Using a Solartron impedance analyzer, the electrical transport characteristics of this pellet were assessed in the frequency range of 100 Hz to 5 MHz. Temperatures between 313 and 353 K were used for the measurements.

3. Results and discussion

3.1. Structure description

Bis(tetrabutylammonium) tetrabromocobaltate(II), $((C_4H_9)_4N)_2[CoBr_4]$, crystallizes in the monoclinic system, space group $P2_1/c$. The refined lattice parameters are: $\beta = 112.185(3)°$, $V = 4206.89(13)$ Å^3, $b = 16.6083(2)$ Å, $c = 16.9298(2)$ Å, and $a = 16.1580(2)$ Å. In this crystal structure, the $[CoBr_4]^{2-}$ anions and the tetrabutylammonium $((C_4H_9)_4N)^+$ cations are linked by strong C–H···Br hydrogen interactions (Fig. 1).

The asymmetric unit of this new hybrid compound consists of a tetrahedral anion $[CoBr_4]^{2-}$ and two crystallographically independent cations $((C_4H_9)_4N)^+$, as illustrated in Fig. 2. The two cations adopt a cis conformation, known as the "swastika" conformation, which corresponds to the most stable configuration. This stability is explained by minimal steric hindrance and optimal arrangement of the butyl chains around the tetrahedral anion.

Such an arrangement is typical of compounds in the A_2MX_4 family, where A represents a bulky organic cation, M a transition metal, and X a halogen. Well-documented examples include $[(C_4H_9)_4N]_2Zn_2Cl_7H_2O$[28] and $[(C_4H_9)_4P]_2SbCl_4$,[29] in

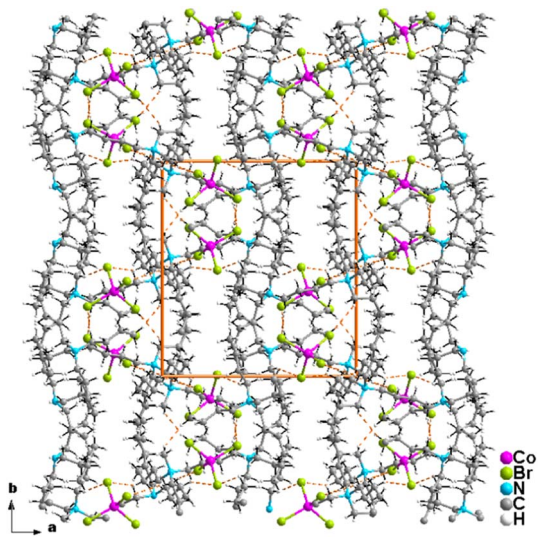

Fig. 1 Projection of the structure of $((C_4H_9)_4N)_2[CoBr_4]$ along the crystallographic c-axis.

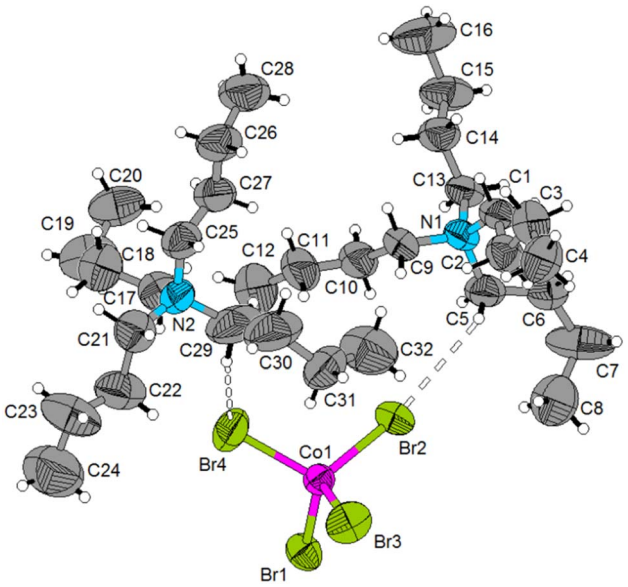

Fig. 2 The asymmetric unit of $(C_{16}H_{36}N)_2[CoBr_4]$. Displacement ellipsoids are drawn at the 50% probability level. Hydrogen bonds are represented by dashed lines.

which the cation generally adopts the cis "swastika" conformation, favoring crystal stability and regular network organization.

The $[CoBr_4]^{2-}$ polyhedron is formed by the coordination of four bromide ions for each Co(II) core. The coordination geometry can be seesaw, square planar, or tetrahedral. In order to measure the departure from an ideal geometry, the τ_4 parameter was computed using the equation,[30] where an ideal tetrahedral configuration is represented by $\tau_4 = 1$ and a perfect square planar geometry by $\tau_4 = 0$.

$$\tau_4 = \frac{360 - (\alpha + \beta)}{360 - 2\theta} \quad (2)$$

where the two largest angles inside the coordination polyhedron are α and β, and θ is the ideal tetrahedral angle ($\theta = 109.5°$). The τ_4 parameter was found to be $\tau_4 = 0.962$ using the measured values of $\alpha = 112.66(5)°$ and $\beta = 111.65(5)°$. This number shows that the geometry of the $[CoBr_4]^{2-}$ polyhedron is quite similar to that of an ideal tetrahedron.

The $[CoBr_4]^{2-}$ anions are stacked in layers to generate anionic pseudo-layers, as seen in Fig. 1, with average planes at $x = \frac{1}{4}$ and $x = \frac{3}{4}$ parallel to the (b, c) plane. The minimal Co···Co intermetallic distance between these layers is 9.7242(13) Å. Co–Br bond lengths range from 2.3953(12) to 2.4253(10) Å within each $[CoBr_4]^{2-}$ unit, and Br–Co–Br bond angles range from 106.63(4)° to 112.66(5)° (Table 3).

Based on the geometrical characteristics of the $[CoBr_4]^{2-}$ tetrahedra, the average Baur distortion indices (DI) were calculated using the following equations:[31]

$$\mathrm{DI(Co-Br)} = \sum_{i=1}^{n_1} \frac{|d_i - d_m|}{n_1 d_m};\ \ \mathrm{DI(Br-Co-Br)} = \sum_{i=1}^{n_2} \frac{|a_i - a_m|}{n_2 a_m} \quad (3)$$

where d represents the Co–Br bond length, a the Br–Co–Br bond angle, d_m and a_m the average values, $n_1 = 4$, and $n_2 = 6$ for tetrahedral environment.

The calculated distortion indices, DI(Co–Br) = 0.0212 and DI(Br–Co–Br) = 0.0191, suggest that the $CoBr_4$ tetrahedron deviates slightly from an ideal tetrahedral geometry. This distortion is attributed to the intermolecular hydrogen bonds formed between the organic cations and the metallic tetrahedra.

The negative charges of the $[CoBr_4]^{2-}$ anions are compensated by tetrabutylammonium cations $((C_4H_9)_4N)^+$, which are arranged in stacked layers forming wavy organic cationic sheets parallel to the (b, c) plane at $x = 0$ and $x = \frac{1}{2}$ (Fig. 1). The crystal structure of the title compound can thus be described as an alternation of organic and inorganic layers along the crystallographic a-axis (Fig. 1).

The geometrical parameters of the organic cations, listed in Table 3, are comparable to those observed in other compounds containing the same organic moiety.[32,33]

The overall stability of the studied crystal lattice relies on weak interactions, notably electrostatic and van der Waals

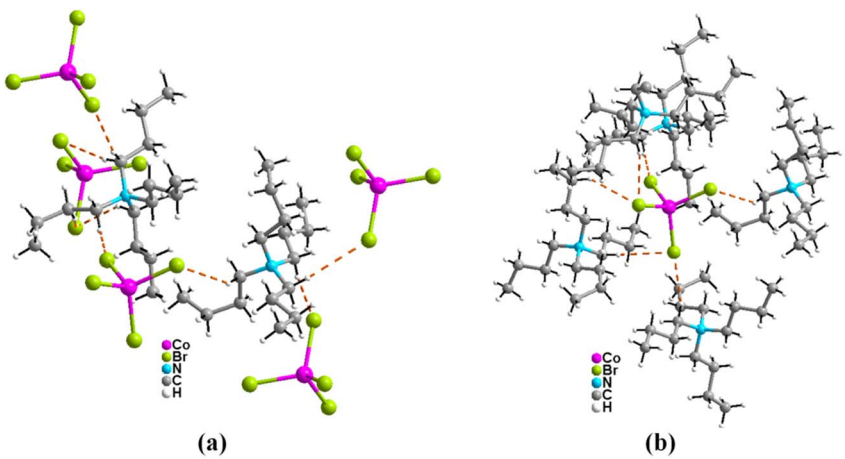

Fig. 3 Hydrogen bonds established by (a) the tetrabutylammonium cations and (b) the metallic tetrahedron in the $[N(C_4H_9)_4]_2CoBr_4$ compound.

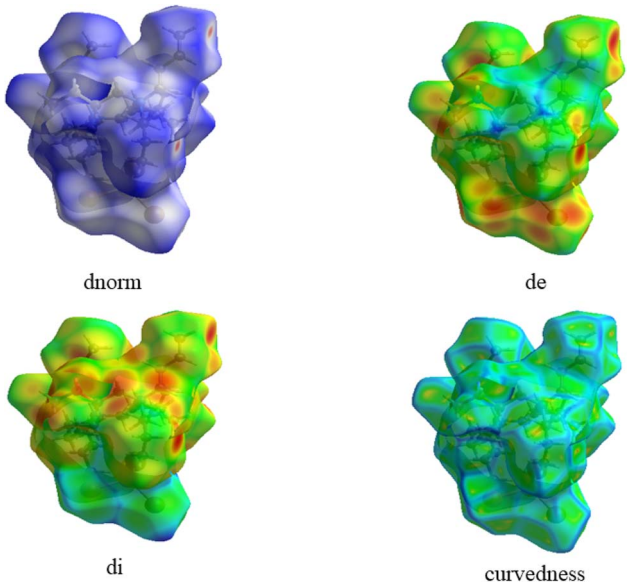

Fig. 4 Hirshfeld surfaces of $[N(C_4H_9)_4]_2CoBr_4$: d_{norm}, d_i, d_e, and curvedness.

interactions, which manifest as C–H···Br hydrogen bonds between tetrabutylammonium cations $((C_4H_9)_4N)^+$ and $[CoBr_4]^{2-}$ anions. Each cation forms C–H···Br interactions with three neighboring $[CoBr_4]^{2-}$ tetrahedra (Fig. 3a), while each $[CoBr_4]^{2-}$ anion interacts with five adjacent tetrabutylammonium cations (Fig. 3b). Although these interactions are relatively weak, they contribute significantly to the cohesion and stability of the lattice. The observed C···Br distances range from 3.748(7) to 4.096(9) Å and the C–H···Br angles vary between 130.2° and 169.4°, confirming the stabilizing role of these intermolecular contacts in the crystal structure (Table 3).

3.2. Hirshfeld surface analysis

To better understand the nature and significance of the intermolecular interactions within the synthesized crystal structure, a Hirshfeld surface analysis was performed. The Hirshfeld surfaces of $[N(C_4H_9)_4]_2CoBr_4$ are illustrated in (Fig. 4). These surfaces, mapped over d_{norm}, are drawn around the molecule to visualize intermolecular contacts. The transparent representation of the surfaces, with appropriate curvature, allows a clear view of the molecular fragments in a consistent orientation for all structures. White regions on the d_{norm} surface correspond to contacts with distances equal to the sum of the van der Waals radii, whereas red and blue areas indicate shorter and longer intermolecular contacts, respectively.

By taking into account both the internal and external nearest neighbors, the three-dimensional Hirshfeld surface can be transformed into a two-dimensional fingerprint plot. This

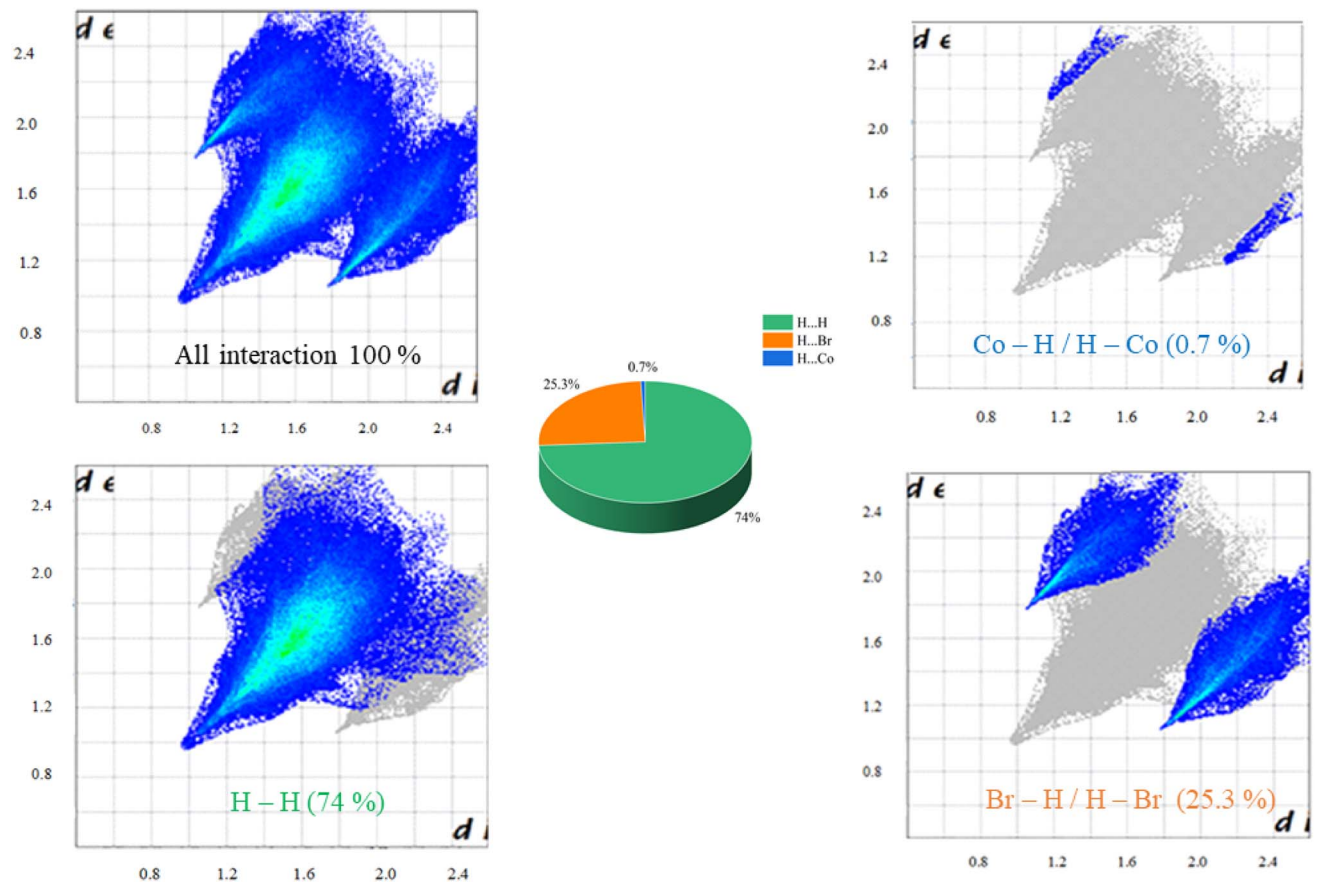

Fig. 5 Fingerprint plot of the proportion of short-range action on the Hirshfeld surface in the $[N(C_4H_9)_4]_2CoBr_4$ compound.

Table 4 Assignments of most important observed bands in infrared and Raman spectra of $[N(C_4H_9)_4]_2CoBr_4$ at room temperature (w: weak; m: mean; s: strong)

Raman (cm^{-1})	IR (cm^{-1})	Assignments
80m	—	$\nu_s(CoBr_4)$
96s	—	$\delta_s(CoBr_4)$
178s	—	$\nu_{as}(CoBr_4)$
238w		
267m	—	$\delta_{as}(CoBr_4)$
744w/785w/809w	738s/801m	$\nu_3(NC_4)$
888m	879s	δ(C–N–C) + δ(C–C–C)
916s	923w	ν_s(NC)
938w	—	ν_s(C–C)
	987w	ν_s(NC) + δ(C–N–C)
1004w/1023w	1007w	δ(C–N–C) + ν(C–C)
1045m	1032m	δ(C–C–C) + δ(C–N–C) + ν(C–C) + δ(N–C–C)
1070m	1062m	δ(C–N–C) + δ(C–C–C)
1123m/1134m	1108w	δ(C–C–C)
1144m		$\tau(CH_2)$
1162m	1167m	$\tau(CH_2)$
1177w		
1191w		
1263w/1283w/1292w	1244w/1282w	$\omega(CH_2)$
1331m/1356w	1316w/1351w	$\omega(CH_2)$ + $\tau(CH_2)$
1366w	1379s	$\omega(CH_2)$
1402w/1414w/1432w/1456s/1463s	1462s	$\delta_{as}(CH_3)$ + sci(CH_2)
1490w		$\delta_{as}(CH_3)$
2879s	2871s	$\nu_s(CH_2)$ + $\nu_s(CH_3)$
2917s	2931s	$\nu_{as}(CH_2)$
2940s/2967s	2958s	$\nu_{as}(CH_3)$
2979s/3000m	2995w	$\nu_{as}(CH_2)$ + $\nu_{as}(CH_3)$

analytical approach enables the differentiation and quantification of various intermolecular interactions, which are collectively displayed in a comprehensive fingerprint representation. The related fingerprint plots are shown in Fig. 5. The two-dimensional fingerprint analysis indicates that the most important interactions in the crystal packing are Br···H/H···Br and H···H, which account for 25.3% and 74.1% of the total surface, respectively. This frequency suggests that maintaining the crystal structure requires van der Waals interactions. The Co···H/H···Co and other minor interactions only account for 0.7% of the Hirshfeld surface contribution.

3.3. Vibrational study at room temperature

Fourier-transform infrared (FT-IR) and Raman spectroscopy were used in vibrational spectroscopic examinations to better understand the molecular structure and the type of chemical bonding inside the $[N(C_4H_9)_4]_2CoBr_4$ molecule. A thorough grasp of the interactions and structural stability of the material is made possible by these complimentary approaches, which offer useful information on the internal vibrations of the crystal's organic and inorganic constituents.

Table 4 summarizes the full vibrational assignment of $[(C_4H_9)_4N]_2$ $CoBr_4$ at room temperature based on comparison with previously published data.[34–37]

The $[(C_4H_9)_4N]^+$ cation is responsible for bands above 400 cm^{-1}, whereas the $[CoBr_4]^{2-}$ anion displays its vibrational modes in the 70–400 cm^{-1} area (Fig. 6).

The Raman bands located at 2879, 2917, 2940, and 2979 cm^{-1} indicate the symmetric and asymmetric C–H stretching vibrations of CH_2 and CH_3 groups in the high-frequency region (2879–3000 cm^{-1}). The infrared bands located at 2871, 2931, 2958, and 2995 cm^{-1} are appropriate for these designations.

Wagging and bending modes are visible in the mid-frequency range. The bending vibrations of CH_2 and CH_3, attributed to wagging (ω) and deformation (δ) modes, are detected at 1366, 1379, 1402, 1414, 1432, 1456, and 1463 cm^{-1}.

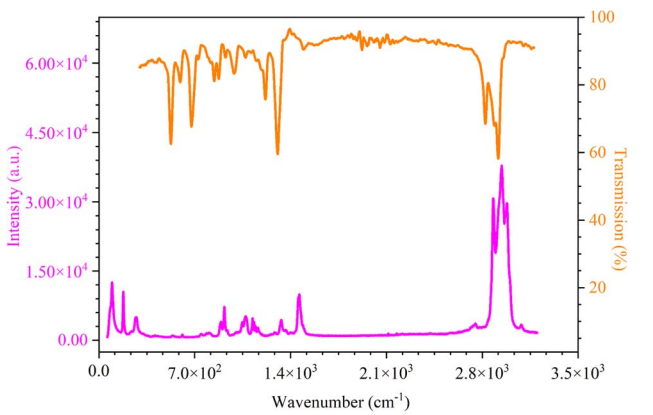

Fig. 6 Raman and IR spectra of $[(C_4H_9)_4N]_2CoBr_4$ compound at room temperature.

The combination of $\delta_{as}(CH_3)$ and CH_2 scissoring is responsible for the strong infrared band at 1462 cm^{-1}. The nitrogen core and butyl chains interact to produce the δ(C–N–C) and δ(C–C–C) vibrations, which are detected at 1065–1070 cm^{-1} in Raman and 1062–1070 cm^{-1} in IR.

Lower-frequency skeletal vibrations involving C–C–C and C–N–C units appear at 1045–1123 cm^{-1} (Raman) and 1032–1108 cm^{-1} (IR). The symmetric stretching of the NC_4 tetrahedral moiety is detected at 738 and 801 cm^{-1} in IR and 744, 785, and 809 cm^{-1} in Raman.

Four fundamental vibrational modes are present in the $[CoBr_4]^{2-}$ anion, which has a normal tetrahedral geometry (T_d symmetry): $\nu_s(CoBr_4)$, $\nu_{as}(CoBr_4)$, $\delta_s(CoBr_4)$, and $\delta_{as}(CoBr_4)$. Below 400 cm^{-1}, the internal modes in the Raman spectra are 80 cm^{-1} (ν_s), 96 cm^{-1} (δ_s), 178 cm^{-1} (ν_{as}), and 267 cm^{-1} (δ_{as}). Additional bending or lattice vibrations of the tetrahedral unit are responsible for the weak bands that are also seen at 238, 538, and 611 cm^{-1}. The tetrahedral coordination of cobalt in the crystal structure is confirmed by these data.

3.4. Thermal analysis

The calorimetric measurement (Fig. 7) showed that the compound under investigation undergoes discontinuation of two phase transitions at $T_1 = 335$ K and $T_2 = 345$ K. The characteristic dynamical values of these phase transitions are listed in Table 5. From the Boltzmann equation, ($\Delta S = R \ln(\Omega)$), where Ω is the rapport number of distinguishable orientations allowed in the high and the low temperature phases (N_1/N_2). The obtained values of Ω were 0.15 and 0.13 at T_1 and T_2, respectively ($\Omega_{1,2} < 2$), which reveals that these two phase transitions are not purely "order–disorder".

3.5. Electrical measurements

The Nyquist spectrum is a powerful tool for analyzing the electrical behavior and ionic dynamics of hybrid materials over a wide range of frequencies and temperatures.[38] It enables distinguishing different transport mechanisms and their contributions. Fig. 8a shows the Nyquist plots of the $[N(C_4H_9)_4]_2CoBr_4$ sample at selected temperatures. The plots exhibit dispersion rather than ideal semicircles centered on the real axis, indicative of Cole–Cole type behavior.[39] The radii of the semicircles decrease with increasing temperature, suggesting enhanced charge transport due to thermal activation, as more charge carriers can overcome energy barriers. This behavior confirms that the compound exhibits semiconductor characteristics[40] with a negative temperature coefficient of resistance (NTCR).[41]

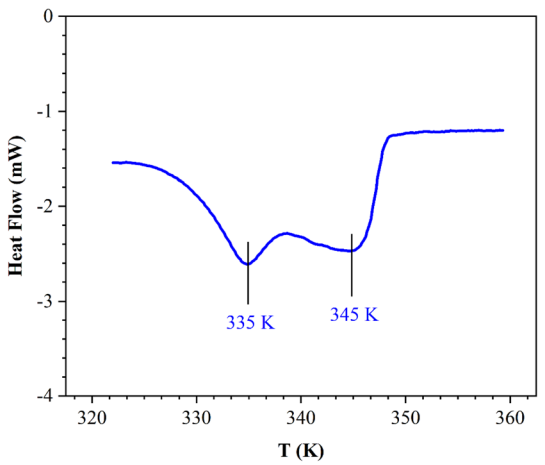

Fig. 7 Differential scattering calorimetric trace of $[(C_4H_9)_4N]_2CoBr_4$.

Table 5 The characteristic dynamical values of $[N(C_4H_9)_4]_2CoBr_4$

T (K)	ΔH (J mol^{-1})	ΔS (J mol^{-1} K^{-1})	Ω
335	163	0.48	0.15
345	141	0.40	0.13

To model the electrical response, an equivalent circuit was proposed for fitting the impedance spectra using ZView software. The optimal fit was achieved with a circuit comprising a parallel combination of global resistance R_1 and a constant phase element (CPE_1), in series with a capacitance C, followed by a parallel combination of global resistance R_2 and CPE_2. The presence of two semicircles corresponds to contributions from grains and grain boundaries. The equivalent circuit model is presented in the inset of Fig. 8a.

To further investigate the frequency-dependent electrical response and relaxation phenomena of the $[N(C_4H_9)_4]_2CoBr_4$ compound, the real and imaginary components of the impedance were analyzed as a function of frequency and temperature. Fig. 8b shows the frequency dependence of the real part of the impedance (Z'). At low frequencies ($f < 5 \times 10^4$ Hz), Z' decreases with increasing temperature and frequency, indicating the accumulation of charge carriers.[42] At higher frequencies ($f > 5 \times 10^5$ Hz), Z' values converge for all temperatures, reflecting the release of space charges. This behavior is consistent with a decreasing effective conduction barrier with rising temperature, leading to reduced resistance and enhanced AC conduction.[43]

The relaxation behavior of the compound is further investigated through the frequency dependence of the imaginary part of the impedance (Z''), as shown in Fig. 8c. Two peaks are observed in the Z'' plots at the relaxation frequencies, satisfying $f_{max}\tau = 1$, indicating contributions from both grains and grain boundaries. These peaks arise from dipolar polarization. The peak positions shift to higher frequencies with increasing temperature, reflecting the temperature-dependent relaxation process[44] and the decreasing resistive character of the sample.[45,46] Additionally, the broadening of the peaks at higher temperatures suggests the presence of a thermally activated electrical relaxation process, associated with immobile electrons at low temperatures and the formation of vacancies at higher temperatures.[47,48]

The resistance values (R) obtained from fitting the impedance spectra were used to calculate the DC conductivity (σ_{DC}) of the grains according to the following equation:

$$\sigma_{DC} = \frac{t}{R \times S} \ (\Omega \ cm)^{-1} \quad (4)$$

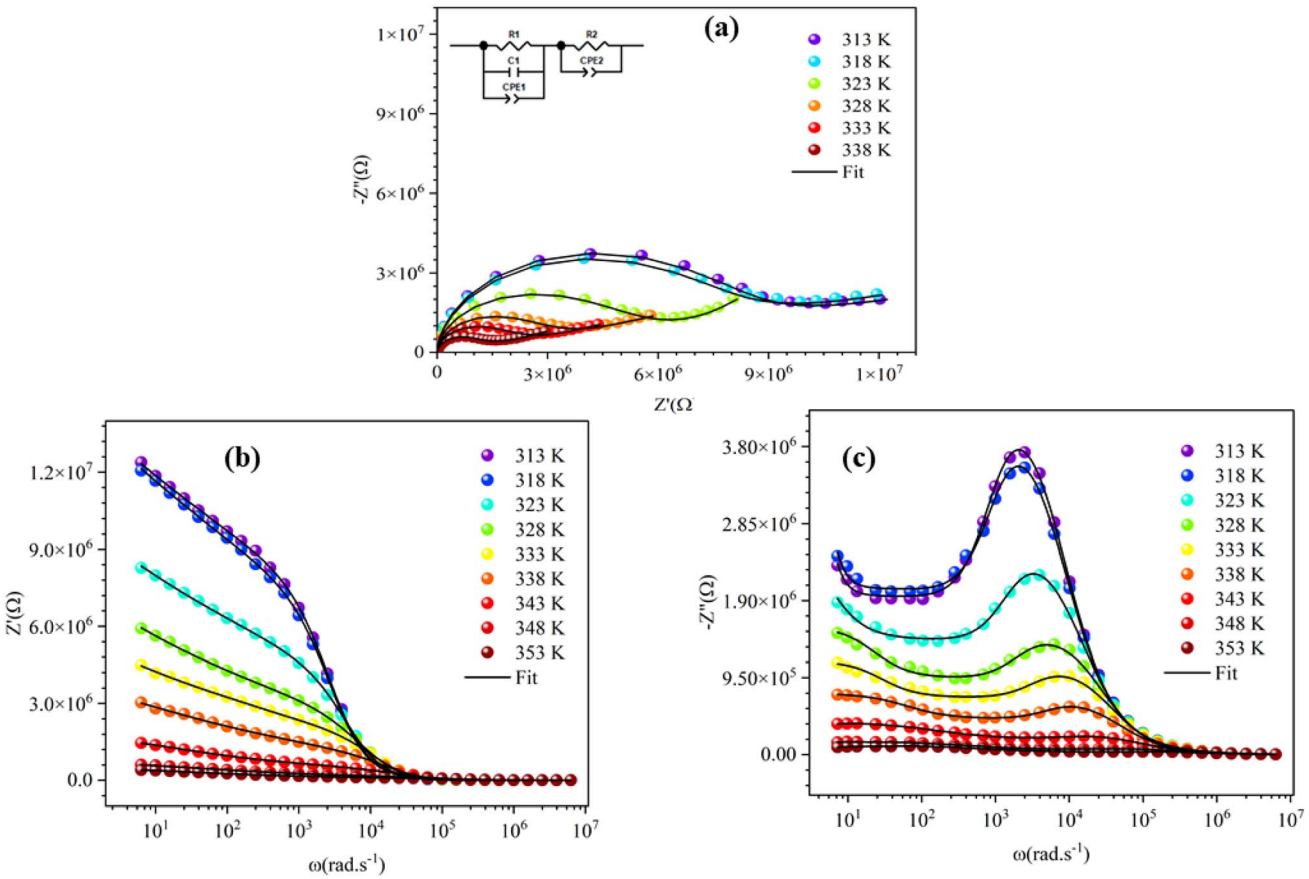

Fig. 8 Complex impedance spectra of $[N(C_4H_9)_4]_2CoBr_4$ at different temperatures: (a) complex impedance spectra, (b) variation of the real part Z' as a function of frequency, and (c) variation of the imaginary part Z'' as a function of frequency.

where t and S are the thickness and the cross-sectional area of the pellet, respectively, and R is the grain resistance.

Fig. 9a shows the variation of the grain conductivity (σ_{DC}) as a function of the inverse absolute temperature. The conductivity increases with temperature, following Arrhenius' law:

$$\sigma_{DC}T = \sigma_0 \exp\left(\frac{-E_a}{k_B T}\right) \quad (5)$$

where σ_0 is the pre-exponential factor, k_B is the Boltzmann constant, and E_a is the activation energy.

Linear fitting of the data revealed two activation energies, $E_{a1} \approx 0.61$ eV in region (I) and $E_{a2} \approx 1.3$ eV in region (II), values comparable to those reported for analogous materials such as $[(C_3H_7)_4N]_2CoBr_4$ (ref. 38) and $[(C_4H_9)_4N]_2Cu_2Cl_6$.[49]

These two activation energies indicate different conduction mechanisms across the temperature range. In the lower-temperature region (I), the relatively small activation energy is consistent with dipole orientation and simple ionic motion. In the higher-temperature region (II), the larger activation energy reflects the onset of more energy-intensive processes, including charge carrier migration. At this stage, partial blockage of electrons due to saturation of conduction sites limits their participation, giving a predominant role to ions and enhancing ionic diffusion.[50] This transition results in a clear modification of the conduction mechanism as the material responds to increasing thermal energy.

To gain insights into charge carrier transport and the dominant conduction mechanisms as a function of temperature and frequency, the electrical conductivity was analyzed using the real (Z') and imaginary (Z'') components of the impedance. The AC conductivity (σ_{AC}) was calculated according to the following equation:[51]

$$\sigma_{AC} = \frac{e}{s}\frac{Z'}{\left(Z'^2 + Z''^2\right)} \quad (6)$$

Fig. 9b shows the AC conductivity spectra of the synthesized compound in the temperature range $313 \leq T \leq 353$ K. Two distinct regions can be identified. At low frequencies, a plateau is observed, corresponding to DC conductivity behavior. At higher frequencies, the AC conductivity increases, defining a dispersive region often referred to as the "conductivity scattering area." This behavior reflects the ability of charge carriers accumulated at grain boundaries to overcome energy barriers as the temperature increases. The low values of σ_{AC} ($\sim 10^{-6}$ Ω^{-1} cm^{-1}) further confirm the semiconducting character of the compound.[52]

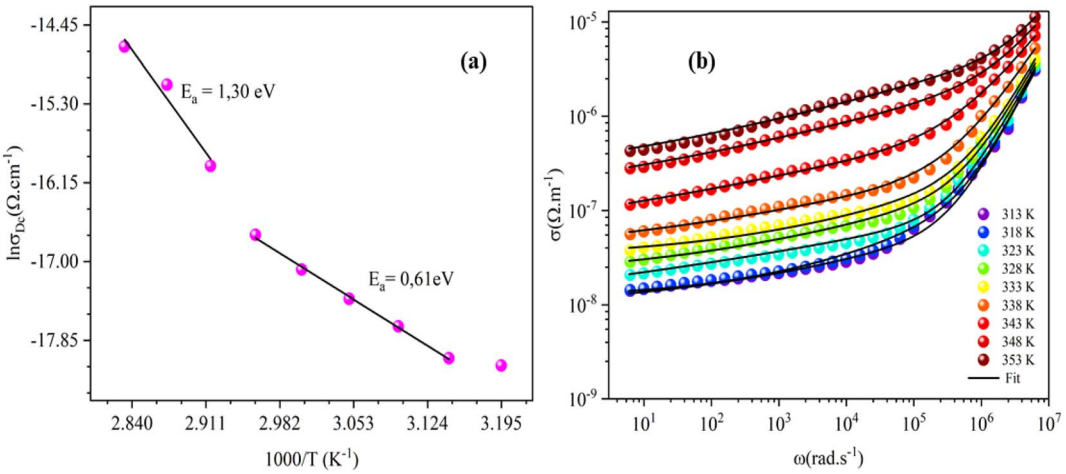

Fig. 9 Temperature dependence of the electrical conductivity of the compound $[(C_4H_9)_4N]_2CoBr_4$: (a) variation of $\ln(\sigma_{DC})$ as a function of 1000/T and (b) evolution of the AC conductivity at different frequencies.

$$\sigma(\omega) = \sigma_{DC} + \sigma_{AC} = \sigma_{DC} + A\omega^{s_1} + B\omega^{s_2} \quad (7)$$

In the following equation, s_1 and s_2 are the frequency exponents, A and B are temperature-dependent constants, and ω is the angular measurement frequency. Each conductivity curve exhibits a dispersive behavior across the frequency range.

To gain further insight into the dynamics of charge carriers in the material, scaling models correlating the conduction mechanisms have been proposed in the literature.[53–55] The conduction mechanism can be inferred from the variation of the frequency exponent s, which reflects the interaction between mobile ions and their local environment, according to Elliott's theory.[56]

Fig. S1 shows the temperature dependence of the exponents s_1 and s_2. The analysis reveals that below 335 K, the conduction behavior is well described by the correlated barrier hopping (CBH) model. Above 335 K, the increase in s_1 and s_2 suggests a transition to a non-overlapping small polaron tunneling (NSPT).

The DSC analysis reveals two distinct thermal events at approximately 335 K and 345 K. In contrast, the electrical measurement shows a single transition centered at 338 K, which corresponds to a clear change in the conduction mechanism. This suggests that both thermal processes detected by DSC manifest as a single, overall modification of the electrical conductivity.

3.6. Dielectric studies with frequency and temperature

The study of the frequency of dielectric properties (Fig. 10) provides essential information on the internal dynamic mechanisms of $[N(C_4H_9)_4]_2CoBr_4$. At low frequencies, the dielectric permittivity of this compound reaches exceptionally high values ($\varepsilon' \approx 10^5$), indicating a predominant contribution from orientational and interfacial polarizations. As the frequency increases, ε' gradually decreases, reflecting the increasing difficulty for charge carriers to keep pace with the rapid changes in the electric field.[57] At high frequencies, the response is mainly controlled by the much faster electronic and ionic polarizations.[58] Compared to other organohalogen compounds, such as $[C_7H_{12}N_2]NiCl_4$ ($\varepsilon' \approx 10^2$)[59] or $[(CH_2)_7(NH_3)_2]CoCl_2Br_2$ ($\varepsilon' \approx 130$),[53] $[N(C_4H_9)_4]_2CoBr_4$ is distinguished by a significantly higher permittivity.[60] This behavior indicates non-Debye relaxation and underscores the material's strong potential for low-frequency energy storage applications,[61] thanks to its exceptional charge retention capacity and the stability of its dielectric response over a wide frequency range. Furthermore, the high polarizability and structural stability of $[N(C_4H_9)_4]_2CoBr_4$ make it a promising candidate for various optoelectronic applications requiring controlled modulation of dielectric properties. Its exceptional characteristics can significantly improve the performance of devices such as electro-optical modulators, photodetectors, or fast-switching components.

The thermal dependence of the dielectric permittivity (ε', Fig. S2) reveals a clear link between molecular dynamics and the material's functional properties. Below 338 K, ε' remains nearly constant, indicating limited reorientation of polarizable entities

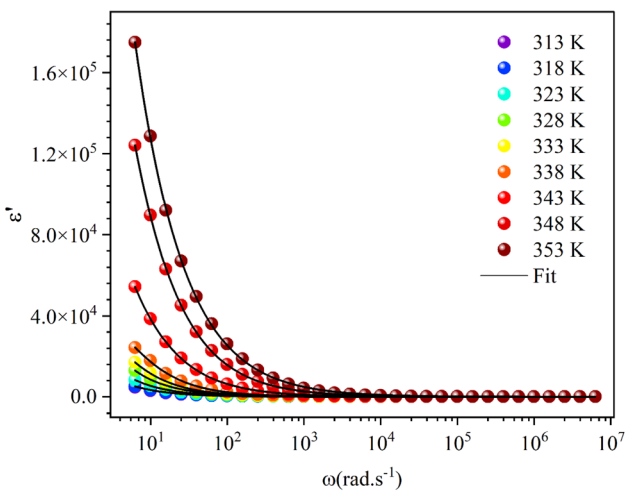

Fig. 10 Frequency-dependent real part of dielectric constant of $[N(C_4H_9)_4]_2CoBr_4$.

and a minor contribution from the organic cations. Above 338 K, thermal activation enhances the rotational mobility of the cations, improving their alignment with the electric field and causing a marked increase in ε'.[62] This sharp change coincides with the phase transition detected by DSC and electrical measurements, demonstrating a direct correlation between structural dynamics and the observed dielectric response.

4. Conclusion

Slow evaporation at room temperature allowed the successful synthesis of a new organic–inorganic hybrid, $[(C_4H_9)_4N]_2[CoBr_4]$, featuring a stable monoclinic ($P2_1/c$) structure in which tetrahedral $[CoBr_4]^{2-}$ units are connected to tetrabutylammonium cations *via* C–H···Br hydrogen bonds. Structural analysis confirms a nearly ideal tetrahedral geometry ($\tau_4 = 0.962$; DI(Co–Br) = 0.0212). Thermal and electrical studies reveal a close correlation between structural changes and transport properties: two nearby thermal events observed by DSC merge into a single electrical transition at 338 K, corresponding to a clear change in conduction mechanism, with activation energies of $E_{a1} = 0.61$ eV and $E_{a2} = 1.3$ eV. AC conductivity analysis further indicates the coexistence of correlated barrier hopping and small polaron tunneling mechanisms. Dielectric measurements highlight exceptionally high low-frequency permittivity ($\varepsilon' \approx 10^5$) and non-Debye relaxation, demonstrating the material's strong dielectric response. Overall, these findings establish $[N(C_4H_9)_4]_2CoBr_4$ as a promising candidate for phase-change devices, low-frequency energy storage, and hybrid electrical applications. Future work will explore temperature-dependent phase behavior and cation/halide substitutions to further optimize its electrical and dielectric properties.

Author contributions

Briki Ridha: writing – original draft, validation, software, methodology, investigation. Ben Brahim Khawla: writing – original draft, formal analysis. Ben Gzaiel Malika: writing – original draft, validation, methodology, review and editing, formal analysis. Nourah A. Alsobai: methodology, review and editing, writing, validation. Rekik Walid: writing – original draft, software, visualization. Abderrazek Oueslati: review and editing, visualization, validation, investigation, formal analysis.

Conflicts of interest

The authors declare that they have no known competing financial interests or personal relationships that could have appeared to influence the work reported in this paper. All persons who have participated in this work are listed as authors.

Data availability

The authors confirm that the data used to support the findings of this study are included within the article and are available from the corresponding author upon reasonable request.

CCDC 2419610 contains the supplementary crystallographic data for this paper.[63]

Supplementary information (SI) is available. See DOI: https://doi.org/10.1039/d5ra09416j.

References

1 S. Burazer, J. Popović, Z. Jagličić, M. Jagodič, A. Šantić, A. Altomare, C. Cuocci, N. Corriero and M. Vrankić, Magnetoelectric coupling springing up in molecular ferroelectric: $[N(C_2H_5)_3CH_3][FeCl_4]$, *Inorg. Chem.*, 2020, **59**(10), 6876–6883.
2 L. Yang, Y. Gao, M. Wu and P. Jena, Interfacial triferroicity in monolayer chromium dihalide, *Phys. Rev. B*, 2022, **105**(9), 094101.
3 R. Lefi, S. Bouzidi, F. Ben Nasr, M. Essid and H. Guermazi, Vibrational study and effect of copper substitution on the electrical properties of the $(C_2H_5NH_3)_2CdCl_4$ hybrid compound, *Inorg. Chem. Commun.*, 2023, **158**, 111374.
4 M. Ben Gzaiel, I. Garoui, F. N. Almutairi, I. Mbarek and A. Oueslati, Lead-free halide perovskites for optoelectronic application: Investigation of structural, optical, electric and dielectric behaviors, *Opt. Mater.*, 2024, **154**, 115664.
5 S. Zaghden, *et al.*, Characterization of a new hybrid compound $(C_3H_8N_6)_2ZnCl_4 \cdot 2Cl$: X-ray structure, Hirshfeld surface, vibrational, thermal stability, dielectric relaxation, and electrical conductivity, *ACS Omega*, 2024, **9**(48), 47597–47612.
6 A. Moulahi, O. Guesmi, M. S. M. Abdelbaky, S. García-Granda and M. Dammak, Structural characterization, thermal analysis, electric and dielectric properties of a novel organic–inorganic hybrid compound based on iron fluoride, *J. Alloys Compd.*, 2022, **898**, 162956.
7 A. Kaiba, F. Al Otaibi, M. H. Geesi, Y. Riadi, T. A. Aljohani and P. Guionneau, A new organic–inorganic hybrid compound $(NH_3(CH_2)C_6H_4CO_2H)[SnCl_6]$: Synthesis, crystal structure, vibrational, optical, magnetic properties and theoretical study, *J. Mol. Struct.*, 2021, **1234**, 130129.
8 H. Chenefa AitYoucef and R. Bourzami, Synthesis, single crystal X-ray structure and vibrational spectroscopic characterization study of a new hybrid material crystal: Bis(2,4,6-trihydroxy-1,3,5-triazin-1-ium) bischloride monohydrate, *J. Mol. Struct.*, 2019, **1191**, 218–224.
9 M. Khalfa, A. Oueslati, K. Khirouni, M. Gargouri, S. Auguste, J. F. Bardeau and G. Corbel, Synthesis, structural and electrical characterization of a new organic–inorganic bromide: $[(C_3H_7)_4N]_2CoBr_4$, *RSC Adv.*, 2022, **12**(5), 2798–2809.
10 A. Ghoudi, I. Chaabane, R. Naouari, A. Aydi, A. Oueslati, E. Dhahri, B. F. O. Costa, T. Nikitin, J. A. Paixão and R. Fausto, Optical and electric properties of the organic–inorganic hybrid bis(2-amino-5-picolinium) tetrachlorocobaltate(II) $[(C_6H_9N_2)_2CoCl_4]$, *Inorg. Chem. Commun.*, 2024, **168**, 112925.
11 M. Ben Gzaiel, R. Briki, S. Znaidia, A. Oueslati and M. Gargouri, Electrical analysis and molecular dynamics of anion in ferroelastic $[(CH_3)_4P]_2CoBr_4$ crystal near high-

temperature phase transitions, *J. Mol. Struct.*, 2024, **1315**, 138810.
12 N. Moutia, A. Oueslati, M. Ben Gzaiel and K. Khirouni, Crystal structure and AC conductivity mechanism of $[N(C_3H_7)_4]_2CoCl_4$ compound, *Phys. E*, 2016, **83**, 88–94.
13 M. Khalfa, New organic–inorganic bromides [(C3H7)4N] 2MBr4 (M=Hg and Cd): Synthesis, crystal structure and vibrational characterization, *J. Alloys Compd.*, 2025, **1034**, 181334.
14 S. Chkoundali and A. Aydi, Electrical conductivity and vibrational studies induced phase transition in $[N(C_3H_7)_4]_2ZnBr_4$ compound, *J. Adv. Dielectr.*, 2021, **11**(1), 2150005.
15 C. Na and A. R. Lim, Elucidation of crystal growth, structural characterization, thermal properties, and molecular dynamics using NMR near phase transition temperature of $[N(CH_3)_4]_2CoCl_4$, *Sci. Rep.*, 2025, **15**(1), 28107.
16 F. Yuan, X. Liu, S. Zhang, P. Zhu, F. Ali, C. Zhao, S. He, Q. Ma, J. Li, K. Guo, L. Li and Z. Wu, Efficient and stable deep-blue 0D copper-based halide $TEA_2Cu_2I_4$ with near-unity photoluminescence quantum yield for light-emitting diodes, *Nanomaterials*, 2024, **14**(23), 1919.
17 H. Elgahami, A. Oueslati, S. Nasr, F. Costantino and H. Naïli, On the high-temperature phase transition of a new chlorocadmate(II) complex incorporating symmetrical Cd_2Cl_6 clusters: Structural, optical and electrical properties, *RSC Adv.*, 2023, **13**(37), 26122–26133.
18 I. Garoui, M. Mallek, F. N. Almutairi, W. Rekik and A. Oueslati, Synthesis, structural characterization and complex impedance analysis of a novel organic–inorganic hybrid compound based on mercury(II) chloride, *J. Mol. Struct.*, 2024, **1315**, 138881.
19 G. M. Sheldrick, *SADABS*, Bruker AXS Inc., Madison, WI, 2002.
20 G. M. Sheldrick, SHELXT: Integrated space-group and crystal-structure determination, *Acta Crystallogr., Sect. A: Found. Adv.*, 2015, **71**(1), 3–8.
21 L. J. Farrugia, WinGXsuite for small-molecule single-crystal crystallography, *J. Appl. Crystallogr.*, 1999, **32**(4), 837–838.
22 G. M. Sheldrick, Crystal structure refinement with SHELXL, *Acta Crystallogr., Sect. C: Struct. Chem.*, 2015, **71**(1), 3–8.
23 *Diamond, Version 3.2i*, Crystal Impact GbR, Bonn, Germany, 2004.
24 O. S. Urgut, *et al.*, New antimony(III) halide complexes with dithiocarbamate ligands derived from thiuram degradation: The effect of the molecule's close contacts on in vitro cytotoxic activity, *Mater. Sci. Eng., C*, 2016, **58**, 396–408.
25 O. S. Urgut, *et al.*, Addition of tetraethylthiuram disulfide to antimony(III) iodide; synthesis, characterization and biological activity, *Inorg. Chim. Acta*, 2016, **443**, 141–150.
26 P. R. Spackman, *et al.*, CrystalExplorer: A program for Hirshfeld surface analysis, visualization and quantitative analysis of molecular crystals, *J. Appl. Crystallogr.*, 2021, **54**(3), 1006–1011.
27 J. J. McKinnon, D. Jayatilaka and M. A. Spackman, Towards quantitative analysis of intermolecular interactions with Hirshfeld surfaces, *Chem. Commun.*, 2007, 3814.
28 M. Ben Gzaiel, A. Oueslati, J. Lhoste, M. Gargouri and A. Bulou, Synthesis, crystal structure and high-temperature phase transition in the new organic–inorganic hybrid $[N(C_4H_9)_4]_3Zn_2Cl_7H_2O$ crystals, *J. Mol. Struct.*, 2015, **1089**, 153–160.
29 H. Elgahami, W. Trigui, A. Oueslati and F. Hlel, Structural, thermal analysis, and electrical conductivity of new organic–inorganic $[(C_4H_9)_4P]SbCl_4$ compound, *Ionics*, 2019, **25**(3), 1359–1371.
30 L. Yang, D. R. Powell and R. P. Houser, Structural variation in copper(I) complexes with pyridylmethylamide ligands: Structural analysis with a new four-coordinate geometry index, τ_4, *Dalton Trans.*, 2007, 955–964.
31 W. H. Baur, The geometry of polyhedral distortions. Predictive relationships for the phosphate group, *Acta Crystallogr., Sect. B: Struct. Crystallogr. Cryst. Chem.*, 1974, **30**(5), 1195–1215.
32 A. R. Lim and K. Y. Lim, Study of phase transition mechanisms in $[N(CH_3)_4]_2ZnCl_4$ by static NMR and MAS NMR, *Solid State Sci.*, 2014, **31**, 70–74.
33 A. Diasse-Sarr, A. H. Barry, L. Diop, R. A. Toscano and B. Mahieu, Spectroscopic studies and crystal structure of tetrabutylammonium trichlorodimethylstannate(IV): $Bu_4NSnMe_2Cl_3$, *C. R. Chim.*, 2007, **10**(6), 469–472.
34 A. Oueslati, F. Hlel and M. Gargouri, Preparation and characterization of organic–inorganic hybrid compound $[N(C_4H_9)_4]_2Cu_2Cl_6$, *Ionics*, 2011, **17**(1), 91–98.
35 M. Ben Gzaiel, A. Oueslati, J. Lhoste, M. Gargouri and A. Bulou, Synthesis, crystal structure and high-temperature phase transition in the new organic–inorganic hybrid $[N(C_4H_9)_4]_3Zn_2Cl_7H_2O$ crystals, *J. Mol. Struct.*, 2015, **1089**, 153–160.
36 W. Trigui, A. Oueslati, F. Hlel and A. Bulou, Raman scattering and alternative current conduction mechanism of the high-temperature phase transition in $[(C_4H_9)_4N]_3Bi_2Cl_9$, *J. Raman Spectrosc.*, 2017, **48**(12), 1718–1724.
37 H. Elgahami, W. Trigui, A. Oueslati and F. Hlel, Structural, thermal analysis, and electrical conductivity of new organic–inorganic $[(C_4H_9)_4P]SbCl_4$ compound, *Ionics*, 2019, **25**(3), 1359–1371.
38 M. Khalfa, A. Oueslati, K. Khirouni, M. Gargouri, A. Rousseau, J. Lhoste, J. F. Bardeau and G. Corbel, Synthesis, structural and electrical characterization of a new organic–inorganic bromide $[(C_3H_7)_4N]_2CoBr_4$, *RSC Adv.*, 2022, **12**, 2798–2806.
39 A. S. Elwakil, A. A. Al-Ali and B. J. Maundy, Extending the double-dispersion Cole–Cole, Cole–Davidson and Havriliak–Negami electrochemical impedance spectroscopy models, *Eur. Biophys. J.*, 2021, **50**(6), 915–926.
40 M. Ben Gzaiel, R. Briki, S. Znaidia, A. Oueslati and M. Gargouri, Electrical analysis and molecular dynamics of anion in ferroelastic $[(CH_3)_4P]_2CoBr_4$ crystal near high-temperature phase transitions, *J. Mol. Struct.*, 2024, **1315**, 138810.
41 L. Thansanga, A. Shukla, N. Kumar and R. N. P. Choudhary, Studies of structural, electrical and ferroelectric

characteristics of gadolinium and yttrium modified bismuth ferrite, *Mater. Chem. Phys.*, 2021, **263**, 124359.

42 H. Elgahami, J. Lhoste, S. Auguste, G. Corbel and A. Oueslati, Structural phase transition, optical and electrical properties of the hybrid material [(C2H5)4N]2ZnI4, *J. Solid State Chem.*, 2022, **314**, 123357.

43 I. Soudani, K. Ben Brahim, A. Oueslati, H. Slimi, A. Aydi and K. Khirouni, Investigation of structural, morphological, and transport properties of a multifunctional Li-ferrite compound, *RSC Adv.*, 2022, **12**(29), 18697–18708.

44 M. Ram, Synthesis and electrical properties of $(LiCo_{3/5}Fe_{1/5}Mn_{1/5})VO_4$ ceramics, *Solid State Sci.*, 2010, **12**(3), 350–354.

45 M. Nadeem and M. J. Akhtar, Melting/collapse of charge orbital ordering and spread of relaxation time with frequency in $La_{0.50}Ca_{0.50}MnO_{3+\delta}$ by impedance spectroscopy, *J. Appl. Phys.*, 2008, **104**(10), 103713.

46 K. Ben Brahim, M. Ben Gzaiel, A. Oueslati and M. Gargouri, Electrical conductivity and vibrational studies induced phase transitions in $[(C_2H_5)_4N]FeCl_4$, *RSC Adv.*, 2018, **8**(71), 40676–40686.

47 I. Garoui, *et al.*, Synthesis, crystal structure, BFDH morphology, Hirshfeld surface analysis and electrical characterization of the new bi-(2-amino-5-methylpyridinium) hexachlorostannate compound, *Phys. E*, 2024, **158**, 115897.

48 P. Dhak, D. Dhak, M. Das, K. Pramanik and P. Pramanik, Impedance spectroscopy study of $LaMnO_3$ modified $BaTiO_3$ ceramics, *Mater. Sci. Eng., B*, 2009, **164**(3), 165–171.

49 A. Oueslati, F. Hlel and M. Gargouri, Preparation and characterization of organic–inorganic hybrid compound $[N(C_4H_9)_4]_2Cu_2Cl_6$, *Ionics*, 2010, **17**(1), 91–98.

50 S. Zaghden, H. Ben Attia, M. S. M. Abdelbaky, A. Oueslati, S. García-Granda, M. Dammak and L. Ktari, Characterization of a new hybrid compound $(C_3H_8N_6)_2ZnCl_4 \cdot 2Cl$: X-ray structure, Hirshfeld surface, vibrational, thermal stability, dielectric relaxation and electrical conductivity, *ACS Omega*, 2024, **9**(48), 47597–47612.

51 Y. Moualhi, H. Rahmouni and K. Khirouni, Usefulness of theoretical approaches and experiential conductivity measurements for understanding manganite transport mechanisms, *Results Phys.*, 2020, **19**, 103570.

52 Y. Moualhi, H. Rahmouni and K. Khirouni, Usefulness of theoretical approaches and experiential conductivity measurements for understanding manganite transport mechanisms, *Results Phys.*, 2020, **19**, 103570.

53 J. Koaib, N. Bouguila, H. Abassi, N. Moutia, M. Kraini, A. Timoumi, C. Vázquez-Vázquez, K. Khirouni and S. Alaya, Dielectric and electrical properties of annealed ZnS thin films: Appearance of the OLPT conduction mechanism in chalcogenides, *RSC Adv.*, 2020, **10**(16), 9549–9562.

54 S. N. Elliott, M. Keçeli, M. K. Ghosh, K. P. Somers, H. J. Curran and S. J. Klippenstein, High-accuracy heats of formation for alkane oxidation: From small to large via the automated CBH-ANL method, *J. Phys. Chem. A*, 2023, **127**(6), 1512–1531.

55 S. R. Elliott, A theory of a.c. conduction in chalcogenide glasses, *Philos. Mag.*, 1977, **36**(6), 1291–1304.

56 A. R. Long, Frequency-dependent loss in amorphous semiconductors, *Adv. Phys.*, 1982, **31**(5), 553–637.

57 B. Nageswara Rao, M. Venkateswarlu and N. Satyanarayana, Electrical and dielectric properties of rare earth oxides coated $LiCoO_2$ particles, *Ionics*, 2014, **20**(2), 175–181.

58 S. Pujaru, P. Maji, P. Sadhukhan, A. Ray, B. Ghosh and S. Das, Dielectric relaxation and charge conduction mechanism in mechanochemically synthesized methylammonium bismuth iodide, *J. Mater. Sci.: Mater. Electron.*, 2020, **31**(11), 8670–8679.

59 D. Abid, I. Mjejri, A. Oueslati, P. Guionneau, S. Pechev, N. Daro and Z. Elaoud, A nickel-based semiconductor hybrid material with significant dielectric constant for electronic capacitors, *ACS Omega*, 2024, **9**, 12743.

60 M. F. Mostafa, S. Abd-Elal and A. K. Tammam, Crystal structure, thermal, electric and magnetic study of $[(CH_2)_7(NH_3)_2]CoCl_2Br_2$, *Indian J. Phys.*, 2014, **88**(1), 49–57.

61 I. Garoui, M. Mallek, F. N. Almutairi, W. Rekik and A. Oueslati, Synthesis, Structural characterization and complex impedance analysis of a novel organic-inorganic hybrid compound based on Mercury (II) chloride, *J. Mol. Struct.*, 2024, **1315**, 138881.

62 A. Elferjani, S. Garcia-Granda and M. Dammak, Synthesis, crystal structure, thermal analysis, dielectric properties and electrical conduction mechanisms of the new mixed solid solution of thallium rubidium sulfate selenate tellurate, *J. Alloys Compd.*, 2018, **749**, 448–464.

63 CCDC 2419610: Experimental Crystal Structure Determination, 2026, DOI: 10.5517/ccdc.csd.cc2m6syl.